Available online at www.sciencedirect.com
ScienceDirect
Trans. Nonferrous Met. Soc. China 29(2019) 1516−1526
Transactions of Nonferrous Metals Society of China
www.tnmsc.cn

Unloading responses of pre-flawed rock specimens under different unloading rates

Xi-bing LI[1], Zheng-hong CHEN[1], Lei WENG[2], Chong-jin LI[1]

1. School of Resources and Safety Engineering, Central South University, Changsha 410083, China;
2. School of Civil Engineering, Wuhan University, Wuhan 430072, China

Received 18 July 2018; accepted 4 March 2019

Abstract: Based on the stress redistribution analysis of rock mass during the deep underground excavation, the unloading process of pre-flawed rock material was simulated by distinct element method (DEM). The effects of unloading rate and flaw inclination angle on unloading strengths and cracking properties of pre-flawed rock specimens are numerically revealed. The results indicate that the unloading failure strength of pre-flawed specimen exhibits a power-function increase trend with the increase of unloading period. Moreover, combined with the stress state analysis on the flaws, it is found that the unloading failure strength increases with the increase of flaw inclination angle. The cracking distribution of pre-flawed specimens under the unloading condition closely depends on the flaw inclination angle, and three typical types of flaw coalescence are observed. Furthermore, at a faster unloading rate, the pre-flawed specimen experiences a sharper and quicker unloading failure process, resulting in more splitting cracks in the specimens.

Key words: deep underground excavation; stress unloading; unloading rate; flaw inclination angle; distinct element method (DEM)

1 Introduction

In deep underground excavations, the excavation unloading process may exert an important effect on the deformation and failure of rock mass [1,2]. The excavation unloading process can be transient or static. If the drill-and-blast (D&B) method is adopted in underground excavations, then the unloading of in-situ stress is a transient process, while the mechanical excavation method is adopted (e.g. road headers, tunnel boring machines (TBM)), the unloading of in-situ stress is a static process [3−5]. The transient unloading process will lead to sudden energy release and severe rock mass failure, resulting a significant effect to the stability of underground engineering [6]. However, the static unloading process is a gradual energy release process, therefore, the mechanical excavation method is considered safer and controllable than the drill-and-blast method during the deep underground excavations [7]. During the mechanical excavation process, the unloading rate of in-situ stress implies the excavation advance rate, a high advance rate can result in a large unloading rate of in-situ stress. Based on the unloading experiments on Beishan granite, ZHAO et al [8] found that the strainburst intensity and the associated acoustic emission (AE) energy release are dependent on the unloading rate, and a higher unloading rate results in a stronger strainburst. HUANG and LI [9] investigated the strain energy conversion of marble under different unloading rates. They concluded that the pre-peak conversion rate of strain energy increases with the unloading rate. Moreover, the failure mode of rock specimen gradually changes from shear to tension with the increase of unloading rate. QIU et al [10] conducted unloading experiments on Jinping marble. Their results indicated that the unloading rate has significant influences on the deformation and failure strength of specimens, and the limited bearing capacity increases with the unloading rate. LI et al [11] numerically investigated the excavation unloading responses of rock around a circular tunnel. They found that the crack number and maximum kinetic energy in the surrounding rock tend to decrease with the decrease of unloading rate.

Foundation item: Projects (41630642, 11472311) supported by the National Natural Science Foundation of China; Project (2017zzts181) supported by the Cultivating Excellent PhDs of Central South University, China; Project (201806370062) supported by the China Scholarship Council
Corresponding author: Zheng-hong CHEN; Tel: +86-15616197001; E-mail: chenzhenghong@csu.edu.cn
DOI: 10.1016/S1003-6326(19)65059-4

These studies help us to realize that the unloading behavior of rock material closely depends on the unloading rate, therefore, during the mechanical excavation process, the choosing of a reasonable excavation advance rate is important. However, so far, studies about unloading rates are mainly focused on intact rock material, while the investigation of unloading rate effects on non-intact rock material is scarce.

It is well known that the engineering rock mass is not necessarily intact and always contains discontinuity structures at multi scales, such as joints, cracks, fissures, weak surfaces, faults, and even artificially induced flaws. In recent years, to analyze the influence of discontinuity structures on the failure of engineering rock mass, rock specimens containing pre-flaws were adopted to reproduce the discontinuity structures in engineering rock mass. Many studies found that the flaw inclination angle of pre-flaws has demonstrated to be a significant factor which influences the strength and failure behavior of rock material. For example, based on numerical simulations, researchers analyzed the cracking process of rock materials containing pre-flaws under uniaxial compression conditions, and they found that flaw inclination angle can significantly affect the crack initiation and propagation process [12−15]. For example, based on laboratory uniaxial compression tests, researchers found that the failure strength and failure mode of pre-flawed rock specimens change with the variation of flaw inclination angle [16−18]. Moreover, by conducting laboratory conventional triaxial compression tests, HUANG et al [19] and YANG et al [20] found that for pre-flawed sandstone and marble specimens, the peak strength and failure mode are depending on not only the confining pressure, but also the geometry of flaw including the flaw inclination angle. However, it needs to be noted that, up to now, the previous studies of strength and failure behavior of pre-flawed rock specimens were mainly carried out under uniaxial or conventional triaxial compression conditions, while the strength and failure behavior of pre-flawed rock specimens under excavation unloading conditions have not been systematically studied.

Nowadays, the numerical simulation plays an important role in investigating the mechanical characteristics of rock materials under different conditions [21−23] owing to its high-efficiency and low cost. In this work, the distinct element method (DEM) was used to investigate the strength and failure behavior of pre-flawed rock specimens under excavation unloading conditions. First, the stress conditions of excavation unloading are analyzed, and the mechanical properties of intact marble are obtained through laboratory compression experiments. Then the intact numerical specimen is calibrated referring to the experiment results of marble specimens. Thereafter, pre-flaws with different inclination angles are created on the calibrated numerical specimen, and a stress variation function based on the stress condition of excavation unloading is encoded in programs to realize the stress unloading at different rates. Finally, the effects of unloading rate and flaw inclination angle on the unloading strength and cracking properties are comprehensively discussed.

2 Background

2.1 Stress conditions of excavation unloading

During the mechanical excavation process in deep underground, the rock mass ahead of the working face undergoes an in-situ stress redistribution process with the advancing of the working face: at first, the rock mass is under a hydrostatic in-situ stress state; then, the horizontal in-situ stress of the rock mass unloads, and the vertical in-situ stress increases to a peak value; finally, the rock mass will suffer the unloading failure (see Fig. 1). This stress redistribution process reflects the realistic stress path for rock mass during deep underground excavation. As shown in Fig. 1, p_0 is the hydrostatic in-situ stress, σ_x is the horizontal in-situ stress, and σ_z is the vertical in-situ stress. The peak stress, which the rock mass suffers before the unloading failure, results from the vertical in-situ stress concentration. The peak stress can be expressed as $\sigma_{z\,\max}=k_1 p_0$, in which k_1 is the stress concentration factor during excavation process. To reproduce the excavation unloading process of rock mass during the deep underground excavation, numerical simulations were performed in this study.

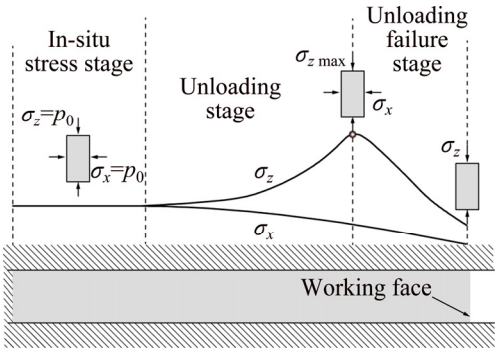

Fig. 1 Excavation unloading stress condition in deep underground mechanical excavation

2.2 Properties of rock material

The rock material investigated in this study is a typical marble and was collected from Leiyang city in Hunan province, China. To obtain the properties of the marble, laboratory uniaxial and conventional triaxial

compression experiments were carried out on the marble specimens. All specimens were cored from the same block of marble, in order to reduce the influence of rock heterogeneity on the experimental results. Moreover, specimens were prepared with dimensions (diameter × height) of 50 mm × 100 mm as recommended by the ISRM [24]. All experiments were conducted on dry specimens at room temperature.

First, using the ISRM suggested method, uniaxial compression experiments were carried out to determine the uniaxial compression strength (UCS), elastic modulus (E) and Poisson's ratio (υ). After that, conventional triaxial compression experiments were performed to obtain the conventional triaxial compression strengths (TCS) at confining pressures (p_0) of 40 MPa (TCS-40), 50 MPa (TCS-50), and 60 MPa (TCS-60). These compression experiments were carried out on servo-controlled test system MTS815, and the load platens loaded at a rate of 0.15 mm/min until the failure of specimen.

Figure 2 and Table 1 summarize the results of the uniaxial and conventional triaxial compression experiments. The stress−strain curves of marble specimens are plotted in Fig. 2(a). It can be seen that specimens underwent brittle failure in post-peak during the uniaxial compression experiment; specimens showed plastic behavior in post-peak during conventional triaxial compression experiments. The failure modes of marble specimens are shown in Fig. 2(b). It can be found that the marble specimen exhibited spalling failure in the uniaxial compression experiment, and shear failure occurred in conventional triaxial compression experiments. The principal stress plot of marble specimens is shown in Fig. 2(c). Accordingly, the corresponding failure criterion parameters of the rock specimen, friction angle (φ) and cohesion (c), were calculated with the Mohr-Coulomb approach.

$$\varphi = 2[\tan^{-1}(\sqrt{B}) - 45],\ c = \frac{\sigma_0}{2\tan(45+\frac{\varphi}{2})} \quad (1)$$

where B is the slope of the principal stresses plot and σ_0 is the uniaxial compression strength (UCS). The Mohr-Coulomb failure criterion parameters are presented in Table 1.

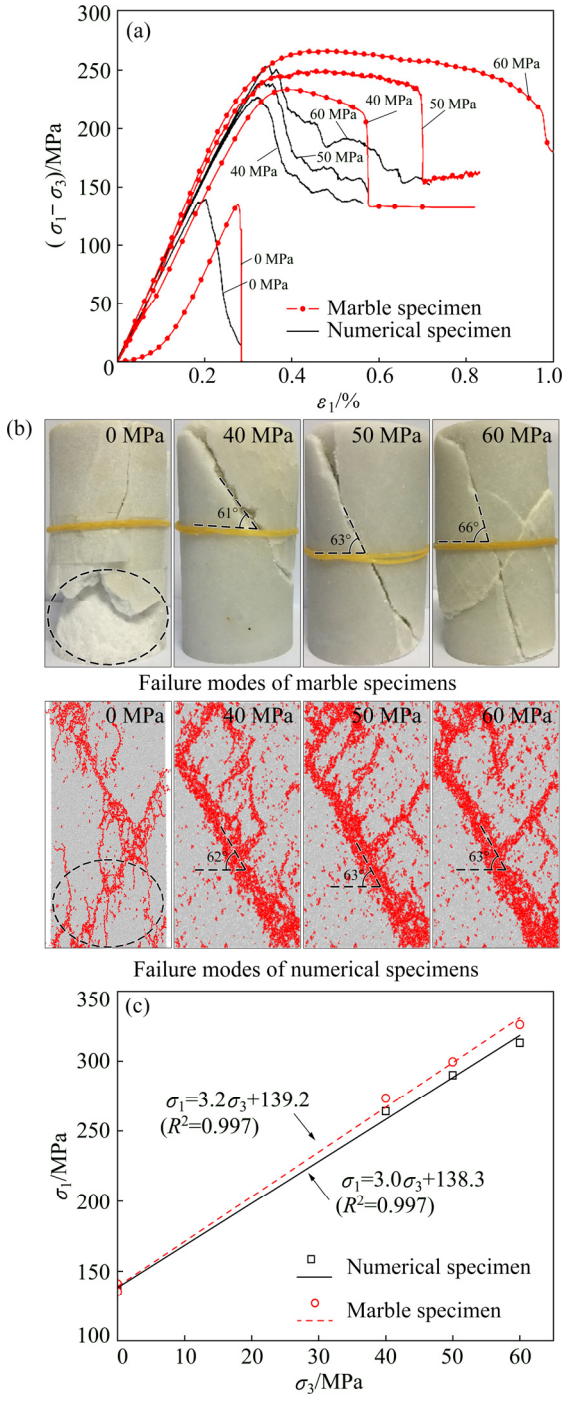

Fig. 2 Uniaxial and conventional triaxial compression tests results of marble specimens and numerical specimens: (a) Stress-strain curves; (b) Fracture modes (red markings indicate microcracks); (c) Principal stress plot

Table 1 Mechanical parameters of marble and numerical specimens

Specimen	Deformation parameter		Compression strength/MPa				Mohr-Coulomb parameter	
	E/GPa	υ	UCS	TCS-40	TCS-50	TCS-60	φ	c
Marble	76.4	0.21	135.3	273.5	299.6	326.1	31.5	37.9
Numerical	75.6	0.21	136.1	264.2	290.0	313.1	30.0	39.3
Error/%	1.0	−	0.59	3.4	3.2	4.0	4.8	3.7

3 Numerical simulation of excavation unloading

3.1 DEM fundamentals

The DEM model based on software Particle Flow Code (PFC, Itasca, Minnesota, USA) mimics the rock material through a collection of grains glued by cement. Each grain in the model is regard as a particle and each cement is regard as a bond. There are two types of bonds, i.e., the contact-bond and parallel-bond. Since the latter has been proved to be more realistic for modelling the brittle rock materials [25,26], the parallel bonded-particle model is used in this study. The properties of the particle−bond system are controlled by the particle−particle contact behavior and the parallel bond behavior. The particle−particle contact behavior and the parallel bond behavior are determined by two sets of micro parameters [27]:

$\left\{E_{\mathrm{c}},(k^{\mathrm{n}}/k^{\mathrm{s}}),\mu\right\}$, microparameters of particle

$\left\{\overline{E}_{\mathrm{c}},(\overline{k}^{\mathrm{n}}/\overline{k}^{\mathrm{s}}),\overline{\lambda},\overline{\sigma}_{\mathrm{c}},\overline{\tau}_{\mathrm{c}}\right\}$, microparameters of parallel bond (2)

where E_{c}, $(k^{\mathrm{n}}/k^{\mathrm{s}})$, μ are the elastic modulus, stiffness ratio of normal stiffness to shear stiffness, and friction coefficient of particle, respectively; $\overline{E}_{\mathrm{c}}$, $(\overline{k}^{\mathrm{n}}/\overline{k}^{\mathrm{s}})$, $\overline{\lambda}$, $\overline{\sigma}_{\mathrm{c}}$ and $\overline{\tau}_{\mathrm{c}}$ are elastic modulus, stiffness ratio of normal stiffness to shear stiffness, ratio multiplier, normal strength, and shear strength of bond, respectively.

The failure criterion of the model is controlled by the parallel bond behavior. The maximum normal and shear stresses acting on the parallel bond can be calculated:

$$\sigma_{\max}=\frac{-\overline{F}^{\mathrm{n}}}{A}+\frac{\left|\overline{M}\right|}{I}\overline{R}$$

$$\tau_{\max}=\frac{\left|\overline{F}^{\mathrm{s}}\right|}{A} \quad (3)$$

where $\overline{F}^{\mathrm{n}}$ is the normal force, $\overline{F}^{\mathrm{s}}$ is the shear force, $\overline{M}$ is the bending moment in parallel bond, A and $\overline{R}$ are the area of bond across section and bond radius, respectively, and I is the moment of inertia. If the maximum normal stress exceeds the normal strength ($\sigma_{\max}\geq\overline{\sigma}_{\mathrm{c}}$) or the maximum shear stress exceeds the shear strength ($\tau_{\max}\geq\overline{\tau}_{\mathrm{c}}$), the parallel bond breaks and hence a microcrack forms.

3.2 Numerical specimen

The numerical specimen is established according to the properties of marble specimen. At first, a particle assembly with height of 100 mm and width of 50 mm was generated. Thereafter, by varying the values of micro parameters as shown in Eq. (2), a series of numerical compression tests were performed on the numerical specimen. During the numerical compression tests, the loading rates of load walls were set as 0.05 m/s until failure happened in the specimens. After a series of "trial and error" calibration tests, a suitable set of microparameters (Table 2) were obtained. Based on this set of microparameters, the calibrated numerical specimen can reproduce the properties of marble specimen.

The comparison of the properties of the calibrated numerical specimen and marble specimen can be seen in Table 1 and Fig. 2. According to Fig. 2(a), the stress−strain curves of calibrated numerical specimen agree well with the laboratorial curves of marble specimen. However, the disagreement which cannot be ignored is that the numerical curves do not show the corresponding post-peak strain platform in conventional triaxial compression tests. Although, there are some disagreements in the post-peak stress−strain curves of numerical specimen and marble specimen, the focuses of this study are on the peak strength and the failure modes. As shown in Fig. 2(b), the failure modes of the numerical specimens are highly consistent with the failure modes of marble specimens: in uniaxial compression test, the failure mode of the numerical specimen is splitting failure; in conventional triaxial compression tests, the failure modes of numerical specimens show shear failures. Moreover, according to the principal stress

Table 2 Microparameters of numerical specimen

Particle microparameter					
Density, ρ/(kg·m^{-3})	Minimum radius, $R_{\min}$/mm	Particle radius ratio, $R_{\max}/R_{\min}$	Elastic modulus, E_{c}/GPa	Friction coefficient, μ	Stiffness ratio, $k^{\mathrm{n}}/k^{\mathrm{s}}$
2820	0.25	1.5	58	0.65	2.5

Parallel bond microparameter						
Elastic modulus, $\overline{E}_{\mathrm{c}}$/GPa	Normal strength, $\overline{\sigma}_{\mathrm{c}}$/MPa	Std. dev. of normal strength/MPa	Shear strength, $\overline{\tau}_{\mathrm{c}}$/MPa	Std. dev. of shear strength/MPa	Stiffness ratio, $\overline{k}^{\mathrm{n}}/\overline{k}^{\mathrm{s}}$	Ratio multiplier, $\overline{\lambda}$
58	94	5	188	5	2.5	1.0

relationships of numerical specimens in compression tests (see Fig. 2(c)), it can be seen that the compression strength of numerical specimens increases lineally with confining pressure; this increasing tendency is similar to that of marble specimen. The mechanical parameters of the calibrated numerical specimen are shown in Table 1. It can be found that the mechanical parameters of numerical specimen, including deformation parameter, compression strength and Mohr-Coulomb parameters, are closely equal to those of marble specimen obtained from laboratory. Based on the comparisons presented in Table 1 and Fig. 2, it can be concluded that the calibrated numerical specimen can reproduce the properties of the marble. Therefore, it is suitable to simulate the marble specimen by the calibrated numerical specimen.

To investigate the unloading behavior of pre-flawed rock specimen, pre-flaws were introduced in the calibrated numerical specimen. In reality, the natural or artificial flaws of rock mass usually show as flaw networks. For simplification, in this study, two straight and open flaws were induced at the center of the numerical specimen. As shown in Fig. 3, the length of two flaws (L_1) is 10 mm, the length of rock bridge (L_2) is 14 mm, the bridge angle (β) is 30°, and the flaw inclination angles (α) are 0°, 30°, 60° and 90°, respectively.

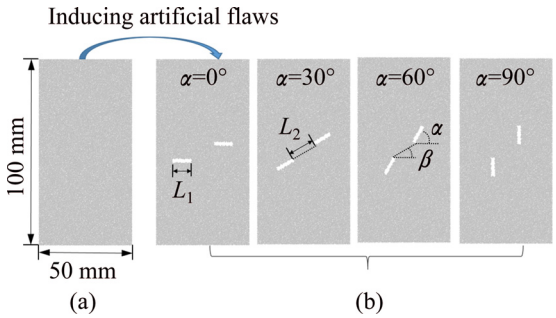

Fig. 3 Inducing artificial flaws: (a) Numerical specimen; (b) Pre-flawed specimens

3.3 Unloading procedures

Based on the stress redistribution process during the underground mechanical excavation described in Section 2.1, the excavation unloading process of rock mass was simulated. The detailed procedures in unloading simulation are as follows:

(1) In-situ stress stage: simultaneously increase the lateral stress (σ_3) and the axial stress (σ_1) to the initial stress level of p_0, and keep them at the initial stress state for a while.

(2) Unloading stage: unload the lateral stress (σ_3) and meanwhile increase the axial stress (σ_1) until the peak stress state of the specimen.

(3) Unloading failure stage: unload the lateral stress (σ_3) to zero, and at this stage the axial stress (σ_1) will spontaneously decrease due to the failure of specimen.

During the unloading simulations, the axial stresses increase at a rate of 0.05 m/s in a displacement controlled manner, and the lateral stresses unload at a linear path in servo controlled manner. The stress path for the lateral stress follows Eq. (4):

$$\sigma_3=\begin{cases} p_0, & 0\le t<t_0 \\ p_0\left(1-\dfrac{t-t_0}{T}\right), & t_0\le t<t_n \end{cases} \tag{4}$$

where p_0 is the initial stress, set as 40 MPa; t is the unloading time; t_0 is the initiation moment of unloading, set as 1 ms; t_n is the end moment of unloading; T is the unloading period.

The linear unloading path is uniform, the influence of different unloading rates can be investigated by means of changing the unloading period. Choosing representative unloading periods is critical, therefore, we considered from two aspects. On one hand, according to LI et al [11], for unloading simulations in the DEM, when unloading time is 2 ms or 5 ms, the disturbance of dynamic unloading observed in the surrounding rock mass during the unloading process is little and can be regard as non-transient unloading. On the other hand, the simulation process in DEM adopts the time-step to calculate, and a critical and reasonable time step was internally assigned in the program before the simulation. In this model, if unloading time is set as 2 ms, then the unloading rate of lateral pressure can be translated to 4.4×10^{-4} MPa /step. It means that 2 ms is low enough to simulate the quasi-static unloading process in the mechanical excavation. Therefore, in this study, the unloading periods (T) of 2, 3, 4 and 5 ms were selected to investigate the influence of different unloading rates on unloading failure responses.

4 Numerical simulation results and discussion

Understanding the stress state and the failure situation of rock mass ahead of the working face during the in-situ stress redistribution process is one of the key components, which enables engineers to determine the optimal excavation scheme. The unloading rate of in-situ stress and the inclination angle of pre-flaws (such as joints, faults or artificially induced flaws) are important factors which can control the stress state and the failure situation of rock mass. The results from this numerical study provide information and insight to allow better understanding of the effects of unloading rate and pre-flaws on the unloading failure behavior, including the unloading strength properties and cracking properties.

4.1 Unloading strength

Figure 4 shows the stress–time curves of pre-flawed specimens under different unloading rates. The unloading rate can be expressed by $v = \Delta\sigma_3 / \Delta t$. It can be seen from Fig. 4 that the shorter the unloading period, the faster the unloading rate ($v_{2\ ms}>v_{3\ ms}>v_{4\ ms}>v_{5\ ms}$). During the unloading process, the axial stress (σ_1) presents a peak strength, which is defined as unloading failure strength (σ_{us}). The corresponding lateral stress (σ_3) at the unloading failure strength is defined as failure lateral stress (σ_{ls}).

To get a better understanding of the failure strength properties of pre-flawed specimens under unloading conditions, more specific and quantitative investigations about the failure strength were carried out. The failure strength of pre-flawed specimens, i.e. the unloading failure strength (σ_{us}) and the lateral failure strength (σ_{ls}), are shown in Fig. 5. According to Fig. 5, it can be seen that at a same flaw inclination angle, the failure strengths (σ_{us} and σ_{ls}) of pre-flawed specimen decrease with the decrease of unloading period. This indicates that the bearing capacity of the rock mass is lower when excavating with a shorter unloading period or a higher rate. Therefore, increasing the excavation advance rate in underground excavation operations will decrease the stress concentration factor (k_1) during the excavation process, resulting in rock mass ahead of the working face failed at a lower strength. On the other hand, at a same unloading period, the unloading failure strength (σ_{us}) of pre-flawed specimen decreases with the decrease flaw inclination angle. Therefore, inducing artificial flaws with a smaller inclination angle will be more efficient to reduce the unloading failure strength of the rock mass. Moreover, the lateral failure stresses (σ_{ls}) of the pre-flawed specimens increase with the flaw inclination angle when the unloading periods are shorter (2 ms or 3 ms). However, at a longer unloading periods (4 ms or 5 ms), the lateral failure stresses (σ_{ls}) of the pre-flawed specimens are nearly the same for different flaw inclination angles. This phenomenon indicates that the failure strength is more obviously influenced by the flaw inclination angle, when the unloading period is shorter.

The specific influences of unloading rate on the unloading failure strength (σ_{us}) are shown in Fig. 6. It can be found that the unloading failure strength of pre-flawed specimens with same flaw inclination angle increases with the increase of unloading period. The possible reasons for such increasing trend are that, at a longer unloading period, the lateral confinement stress on the pre-flawed specimens is larger ($\sigma_{ls\ 2\ ms}>\sigma_{ls\ 3\ ms}>\sigma_{ls\ 4\ ms}>\sigma_{ls\ 5\ ms}$) and the unloading disturbance is smaller, hence resulting in larger unloading failure strength. The relationship of unloading failure strength and unloading period is as follows:

$$\sigma_{us}=aT^{b}\quad (a>0,\ 0<b<1) \tag{5}$$

where a and b are the coefficients, the value of b is larger than 0.0 and smaller than 1.0, which means that the increasing tendency of unloading failure strength tends gentle with the increase of unloading period.

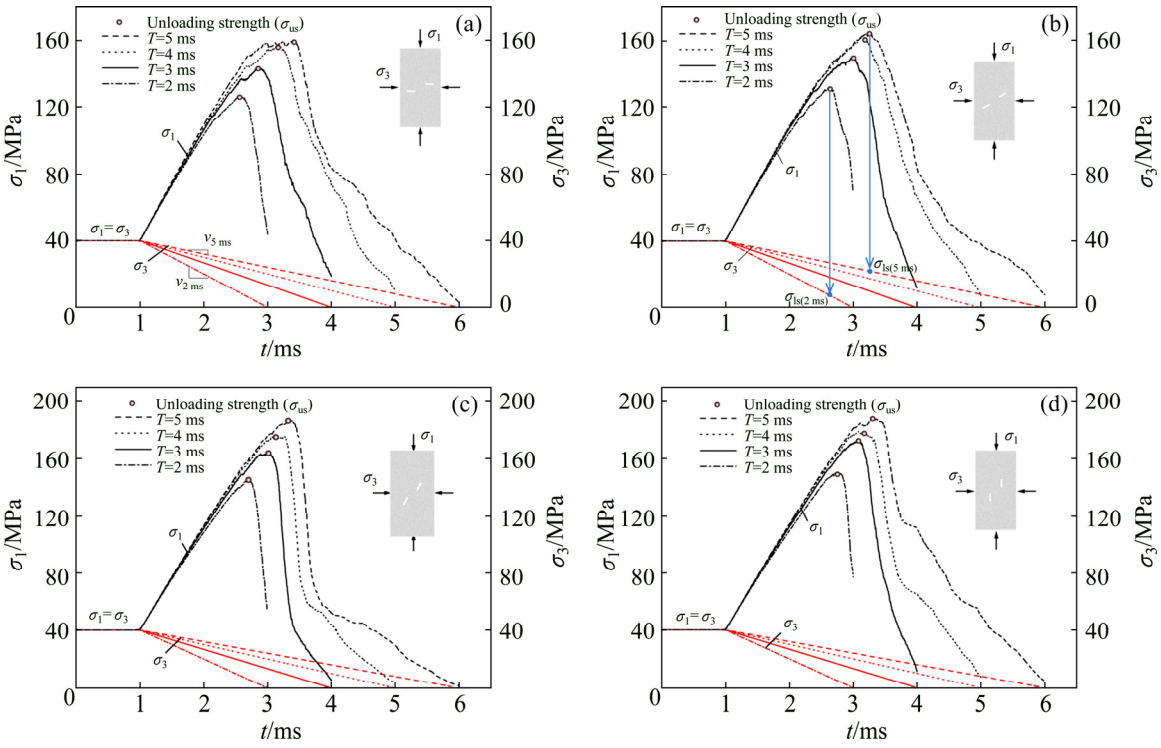

Fig. 4 Stress–time curves of pre-flawed specimens during unloading simulations: (a) α=0°; (b) α=30°; (c) α=60°; (d) α=90°

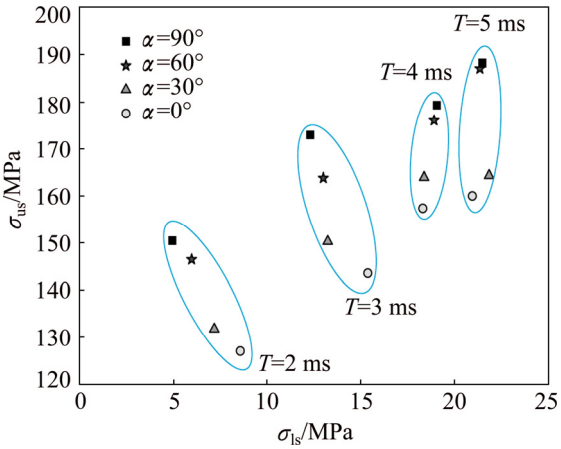

Fig. 5 Relationship between unloading failure strength and failure lateral stress

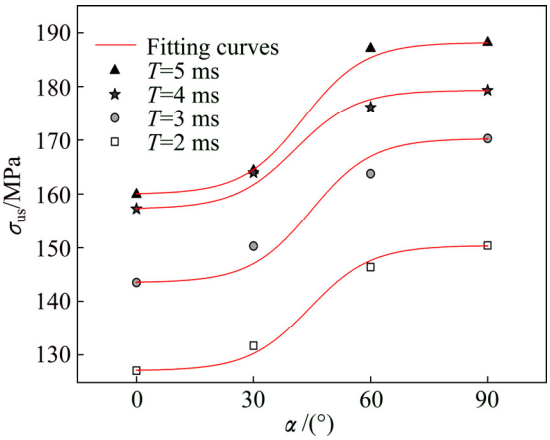

Fig. 7 Relationship between unloading strength and flaw inclination angle

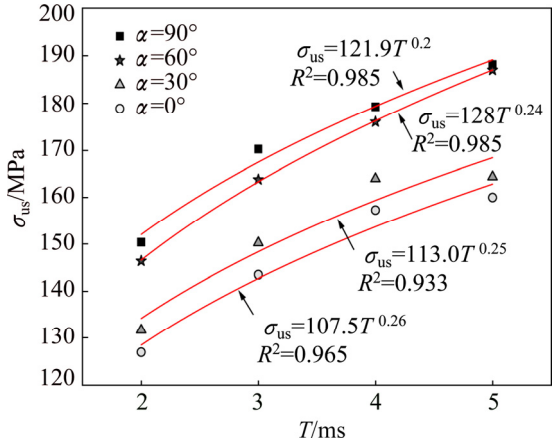

Fig. 6 Relationship between unloading strength and unloading period

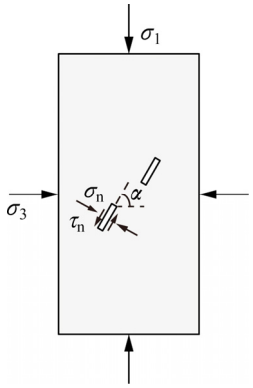

Fig. 8 Stress state sketch on pre-flaws

The influences of flaw inclination angle on the unloading failure strength are shown in Fig. 7. It can be found that for pre-flawed specimens at same unloading period, the unloading failure strength exhibits an "S" shape rising trend with the increase of flaw inclination angle. To further explain the effect of flaw inclination angle on the unloading failure strength, the stress states on flaws were theoretically analyzed. The stress state sketch on pre-flaw is shown in Fig. 8. Through a stress analysis, the effective normal stress σ_n and the effective shear stress τ_n on the flaw surface can be obtained.

$$\begin{cases} \sigma_n = \sigma_1 \cos^2\alpha + \sigma_3 \sin^2\alpha \\ \tau_n = \dfrac{\sigma_1 - \sigma_3}{2} \sin 2\alpha \end{cases} \tag{6}$$

where α is the flaw inclination angle, σ_1 and σ_3 are the axial and lateral stresses, respectively.

By substituting α=0°, 30°, 60° and 90° into Eq. (6), the effective normal and effective shear stresses on the flaws can be calculated. It should be noted that the flaws are open and slender, which means that the effective normal stresses on the flaws can make the flaw to close and induce tensile stress at the flaws, resulting in tensile cracks around the flaws. The effective shear stresses on the flaws can result in shear cracks around the flaw. Figure 9 shows the results of the effective normal and shear stresses on the flaws with different inclination angles at the unloading period of 2 ms. According to Fig. 9, it can be found that compared with other flaws, the flaws at inclination angle of 0° suffer the largest normal stress ($\sigma_{n(0^\circ)}$), and the shear stress is zero ($\tau_{n(0^\circ)} = 0$). In this regard, tensile cracks are most likely to initiate and propagate around the flaws at inclination angle of 0°, which results in the lowest failure strength of the specimen. For flaws at inclination of 30°, the normal stress is larger than the shear stress ($\sigma_{n(30^\circ)} > \tau_{n(30^\circ)}$). For flaws at inclination of 60°, the shear stress is larger than the normal stress ($\tau_{n(60^\circ)} > \sigma_{n(60^\circ)}$). For flaws at inclination of 90°, the shear stress is zero ($\tau_{n(90^\circ)} = 0$) and the normal stress ($\sigma_{n(90^\circ)}$) is the smallest and

decreasing. This means that for flaws with inclination angle of 90°, the effective stresses on the flaws will not result in significant cracking phenomenon. Therefore, the specimen with inclination angle of 90° failed as a whole and not influenced by the flaws, and this is the reason why its unloading failure strength is the highest.

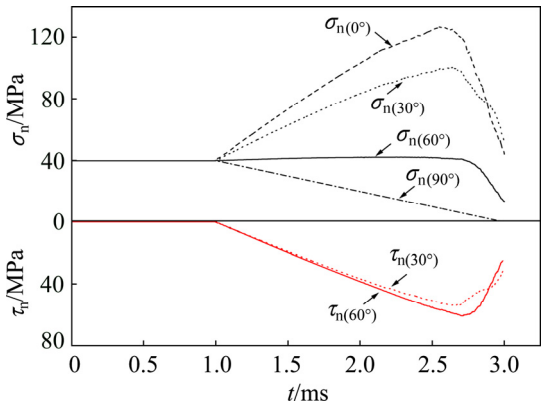

Fig. 9 Normal and shear stresses on flaws with different inclination angles (T= 2 ms)

4.2 Unloading cracking

To understand the fracture behavior of pre-flawed specimen under unloading condition, the cracking properties of pre-flawed specimens at different unloading rates and flaw inclination angles were analyzed from the perspective of flaw coalescence behavior and crack distribution. The coalescence is produced by the linkage of two flaws through cracks. The coalescence behavior is vital for the failure of the pre-flawed specimen and is influenced by the flaw inclination angle. The classifications of coalescence types under compression condition are available in many literatures [28−30]. Based on the present study, the flaw coalescence behavior of pre-flawed specimens under unloading condition was investigated. Three typical types of flaw coalescence were observed, i.e., the direct coalescence, indirect coalescence and no coalescence. As shown in Fig. 10, for the direct coalescence, the coalescence is along the direction of the rock bridge, and for the indirect coalescence, the coalescence is away from the direction of the rock bridge.

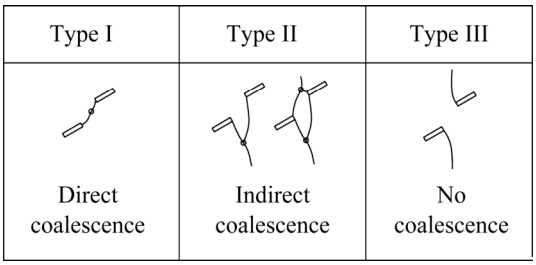

Fig. 10 Three typical types of flaw coalescence

The coalescence types and crack distributions of pre-flawed specimens at the end of unloading are shown in Fig. 11. It can be seen in Fig. 11 that for pre-flawed specimens with α=0°, the flaws exhibit indirect coalescence at any unloading rate; at the same time, cracks mainly distribute and propagate along the flaw tips and flaw surfaces. This is because for specimens with α=0°, cracks are easily to initiate and propagate along the pre-flaws. For specimens with α=30°, the flaws exhibit three different types of coalescences under different unloading periods; moreover, many cracks

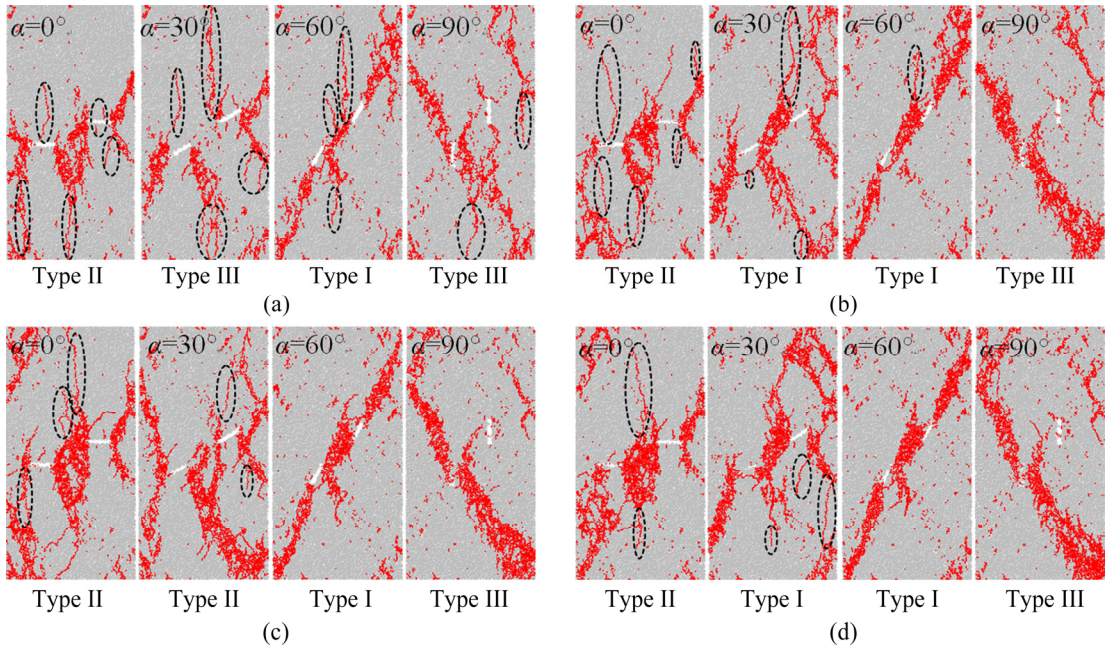

Fig. 11 Fracture results of pre-flawed specimens under unloading conditions: (a) T=2 ms; (b) T=3 ms; (c) T=4 ms; (d) T=5 ms

distribute and propagate around the flaw tips. For specimens with α=60°, at different unloading rates, the coalescence types of the flaws are all direct coalescence; furthermore, the distribution of cracks forms a shear band whose tilt angle is same as the flaw inclination angle. For pre-flawed specimens with α=90°, there are no coalescences between the flaws; moreover, the crack distributions of the specimens are not mainly around the flaws, instead, the cracks formed a shear failure band, just like the failure mode of intact specimens in conventional triaxial compression tests. This kind of crack distribution can be explained by the stress state of flaws: for flaws at α=90°, the effective normal stress on the flaws decreases and the effective shear stress is zero, therefore, the formation of cracks is not controlled by the flaws. According to the above cracking properties analyses, it can be concluded that the flaw coalescences for specimens with α=0°, 60° and 90° are not influenced by the unloading periods, while the flaw coalescences for specimens with α=30° are obviously influenced by the unloading period. Therefore, if the rock mass ahead of the working face contains natural flaws whose inclination angle is 30°, engineers should be more careful during excavation processes, because the coalescence behavior of natural flaws is complex and unpredictable. Moreover, the overall cracking distributions are generally similar for the pre-flawed specimens with varying unloading periods, while the overall cracking distributions are obviously different for pre-flawed specimens with varying flaw inclination angles. This phenomenon indicates that under unloading conditions, the flaw inclination angle plays a more important effect on the cracking distributions of pre-flawed specimens than the unloading rate.

Although the overall cracking distribution of pre-flawed specimen is less related to the unloading rate, it is obvious that there are more axial splitting cracks when the pre-flawed specimens are unloaded at faster unloading rates. The axial splitting cracks are parallel to the axial direction and marked by dashed lines in Fig. 11. The occurrence of splitting cracks indicates that the failure of the specimen is brittle and quite quick [31]. In this study, the axial splitting cracks mean that the failure process is more brittle and quick for pre-flawed specimen at a faster unloading rate. To verify this phenomenon, the built-in energy tracing module was activated to track the released kinetic energy, E_k, of specimens. As shown in Fig. 12, the kinetic energy evolutions of specimens with α=0° indicate that the peak kinetic energy will increase with the increase of unloading rate. In addition, for the specimen unloaded at a faster unloading rate, the release process of kinetic energy is a more sudden process. Therefore, it can be concluded that the specimen will experience a sharper and more sudden failure response and energy evolution when the unloading rate is faster. This conclusion indicates that the failure and energy evolution process of rock mass ahead of the working face can be controlled by the excavation advance rate.

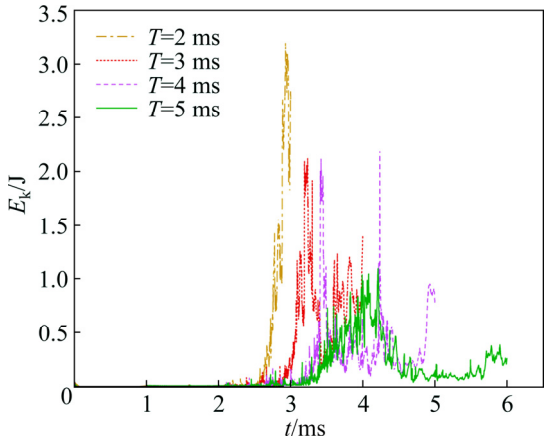

Fig. 12 Kinetic energy evolution of pre-flawed specimens at different unloading periods (α=0°)

5 Conclusions

(1) The unloading failure strength of pre-flawed specimen exhibits a power-function increase trend with the increase of unloading period. Moreover, with the increase of flaw inclination angle, the unloading failure strength increases in a "S" shape, and this increasing tendency is verified by the stress state analysis on the flaws.

(2) The cracking properties of pre-flawed specimen under unloading condition closely depend on the flaw inclination angle. At any given unloading rate, three typical types of flaw coalescences were observed in specimens with different flaw inclination angles. Furthermore, at a faster unloading rate, the pre-flawed specimens will experience sharper energy evolution and unloading failure process, resulting in more splitting cracks in the specimen.

(3) From the perspective of applications, the present work can provide some useful information for mechanical excavation in deep underground engineering. First, increasing the excavation advance rate in underground excavation operations will decrease the stress concentration factor during excavation process, resulting in the rock mass ahead of the working face failed at a lower strength. Second, inducing artificial per-flaws with a smaller inclination angle in the rock mass ahead of the working face will be more efficient to reduce the unloading failure strength. Third, the unloading cracking characteristics of rock mass containing pre-flaws can be predicted according to the flaw inclination angle. The failure and the energy

evolution process of rock mass ahead of the working face can be controlled by the excavation advance rate.

References

[1] CAO W, LI X, TAO M, ZHOU Z. Vibrations induced by high initial stress release during underground excavations [J]. Tunnelling and Underground Space Technology, 2016, 53: 78−95.

[2] YANG J, LU W, HU Y, CHEN M, YAN P. Numerical simulation of rock mass damage evolution during deep-buried tunnel excavation by drill and blast [J]. Rock Mechanics and Rock Engineering, 2015, 48: 2045−2059.

[3] FAN Y, LU W, ZHOU Y, YAN P, LENG Z, CHEN M. Influence of tunneling methods on the strainburst characteristics during the excavation of deep rock masses [J]. Engineering Geology, 2016, 201: 85−95.

[4] LI X, LI C, CAO W, TAO M. Dynamic stress concentration and energy evolution of deep-buried tunnels under blasting loads [J]. International Journal of Rock Mechanics and Mining Sciences, 2018, 104: 131−146.

[5] ZHU W C, WEI J, ZHAO J, NIU L L. 2D numerical simulation on excavation damaged zone induced by dynamic stress redistribution [J]. Tunnelling and Underground Space Technology, 2014, 43: 315−326.

[6] ZHAO X G, CAI M. Influence of specimen height-to-width ratio on the strainburst characteristics of Tianhu granite under true-triaxial unloading conditions [J]. Canadian Geotechnical Journal, 2014, 52: 890−902.

[7] HARTLIEB P, GRAFE B, SHEPEL T, MALOVYK A, AKBARI B. Experimental study on artificially induced crack patterns and their consequences on mechanical excavation processes [J]. International Journal of Rock Mechanics and Mining Sciences, 2017, 100: 160−169.

[8] ZHAO X G, WANG J, CAI M, CHENG C, MA L K, SU R, ZHAO F, LI D J. Influence of unloading rate on the strainburst characteristics of beishan granite under true-triaxial unloading conditions [J]. Rock Mechanics and Rock Engineering, 2014, 47: 467−483.

[9] HUANG D, LI Y. Conversion of strain energy in triaxial unloading tests on marble [J]. International Journal of Rock Mechanics and Mining Sciences, 2014, 66: 160−168.

[10] QIU Shi-li, FENG Xia-ting, ZHANG Chuan-qing, ZHOU Hui, SUN Feng. Experimental research on mechanical properties of deep-buried marble under different unloading rates of confining pressures [J]. Chinese Journal of Rock Mechanics & Engineering 2010, 29: 1807−1817. (in Chinese)

[11] LI X, CAO W, ZHOU Z, ZOU Y. Influence of stress path on excavation unloading response [J]. Tunnelling and Underground Space Technology, 2014, 42: 237−246.

[12] ZHANG X P, WONG L N Y. Crack initiation, propagation and coalescence in rock-like material containing two flaws: A numerical study based on bonded-particle model approach [J]. Rock Mechanics and Rock Engineering, 2013, 46: 1001−1021.

[13] LIU T, LIN B, ZOU Q, ZHU C, YAN F. Mechanical behaviors and failure processes of precracked specimens under uniaxial compression: A perspective from microscopic displacement patterns [J]. Tectonophysics, 2016, 672−673: 104−120.

[14] MANOUCHEHRIAN A, SHARIFZADEH M, MARJI M F, GHOLAMNEJAD J. A bonded particle model for analysis of the flaw orientation effect on crack propagation mechanism in brittle materials under compression [J]. Archives of Civil and Mechanical Engineering, 2014, 14: 40−52.

[15] ZHAO Z, ZHOU D. Mechanical properties and failure modes of rock samples with grout-infilled flaws: A particle mechanics modeling [J]. Journal of Natural Gas Science and Engineering, 2016, 34: 702−715.

[16] LEE H, JEON S. An experimental and numerical study of fracture coalescence in pre-cracked specimens under uniaxial compression [J]. International Journal of Solids and Structures, 2011, 48: 979−999.

[17] WONG L N Y, EINSTEIN H H. Systematic evaluation of cracking behavior in specimens containing single flaws under uniaxial compression [J]. International Journal of Rock Mechanics and Mining Sciences, 2009, 46: 239−249.

[18] WONG R H C, CHAU K T. Crack coalescence in a rock-like material containing two cracks [J]. International Journal of Rock Mechanics and Mining Sciences, 1998, 35: 147−164.

[19] HUANG D, GU D, YANG C, HUANG R, FU G. Investigation on mechanical behaviors of sandstone with two preexisting flaws under triaxial compression [J]. Rock Mechanics and Rock Engineering, 2016, 49: 375−399.

[20] YANG S Q, JIANG Y Z, XU W Y, CHEN X Q. Experimental investigation on strength and failure behavior of pre-cracked marble under conventional triaxial compression [J]. International Journal of Solids and Structures, 2008, 45: 4796−4819.

[21] ZHOU Z L, ZHAO Y, JIANG Y H, ZOU Y, CAI X, LI D Y. Dynamic behavior of rock during its post failure stage in SHPB tests [J]. Transactions of Nonferrous Metals Society of China, 2017, 27: 184−196.

[22] XIA M. Thermo-mechanical coupled particle model for rock [J]. Transactions of Nonferrous Metals Society of China, 2015, 25: 2367−2379.

[23] YIN T, ZHANG S, LI X, BAI L. A numerical estimate method of dynamic fracture initiation toughness of rock under high temperature [J]. Engineering Fracture Mechanics, 2018, 204: 87−102.

[24] ULUSAY R. The ISRM suggested methods for rock characterization, testing and monitoring: 2007−2014 [M]. Switzerland: Springer International Publishing, 2015.

[25] FAKHIMI A. Application of slightly overlapped circular particles assembly in numerical simulation of rocks with high friction angles [J]. Engineering Geology, 2004, 74: 129−138.

[26] CHO N, MARTIN C D, SEGO D C. A clumped particle model for rock [J]. International Journal of Rock Mechanics and Mining Sciences, 2007, 44: 997−1010.

[27] ITASCA C G. Users' manual for particle flow code in 2 dimensions (PFC2D): Version 3.1 [M]. Minneapolis: Itasca, 2002.

[28] BOBET A, EINSTEIN H H. Fracture coalescence in rock-type materials under uniaxial and biaxial compression [J]. International Journal of Rock Mechanics and Mining Sciences, 1998, 35: 863−888.

[29] SAGONG M, BOBET A. Coalescence of multiple flaws in a rock-model material in uniaxial compression [J]. International Journal of Rock Mechanics and Mining Sciences, 2002, 39: 229−241.

[30] WONG L N Y, EINSTEIN H H. Crack coalescence in molded gypsum and carrara marble: Part 1. Macroscopic observations and interpretation [J]. Rock Mechanics and Rock Engineering, 2009, 42: 475−511.

[31] HAN L, HE Y, ZHANG H. Study of rock splitting failure based on Griffith strength theory [J]. International Journal of Rock Mechanics and Mining Sciences, 2016, 83: 116−121.

不同卸载速度下含裂隙岩体的卸载响应

李夕兵[1]，陈正红[1]，翁 磊[2]，黎崇金[1]

1. 中南大学 资源与安全工程学院，长沙 410083；
2. 武汉大学 土木工程学院，武汉 430072

摘 要：基于深部开挖过程中的应力重分布分析，利用离散元方法(DEM)对卸载过程进行模拟，揭示卸载条件下卸载速度和裂隙倾角对含裂隙岩体的强度和裂纹特性的影响。结果表明：随着卸载周期的增大，含裂隙岩体的卸载破坏强度呈幂函数增大。同时，结合缺陷上的应力分析发现，含裂隙岩体的卸载破坏强度随着裂隙倾角的增大逐渐增大；卸载条件下含裂隙岩体的裂纹分布主要取决于裂隙倾角，并总结了 3 种不同的裂隙搭接方式；此外，卸载速度越快，含裂隙岩体的卸载破坏过程越剧烈，岩体内部形成的劈裂裂纹越多。

关键词：深部开挖；应力卸载；卸载速度；裂纹倾角；离散元方法

(Edited by Xiang-qun LI)